IEEE Photonics Journal
An IEEE Photonics Society Publication

Open Access

Orthogonal Time-Frequency Multiplexing With 2D Hermitian Symmetry for Optical-Wireless Communications

Volume 12, Number 2, April 2020

Jie Zhong
Ji Zhou
Weiping Liu
Jiayin Qin

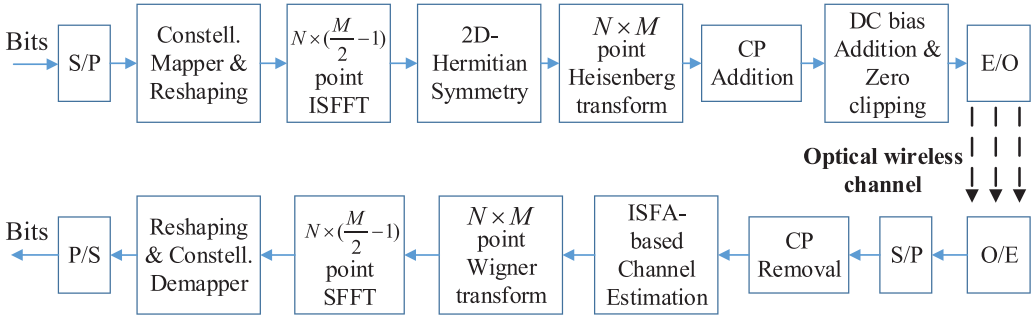

Block diagram of DCO-OTFM OWC system

DOI: 10.1109/JPHOT.2020.2972587

Orthogonal Time-Frequency Multiplexing With 2D Hermitian Symmetry for Optical-Wireless Communications

Jie Zhong,[1] **Ji Zhou**,[2] **Weiping Liu**,[2] **and Jiayin Qin**[1]

[1]School of Electronics and Information Technology, Sun Yat-sen University, Guangzhou 510006, China
[2]Department of Electronic Engineering, College of Information Science and Technology, Jinan University, Guangzhou 510632, China

DOI:10.1109/JPHOT.2020.2972587

Manuscript received December 25, 2019; revised February 4, 2020; accepted February 5, 2020. Date of publication February 9, 2020; date of current version March 9, 2020. This work was supported in part by the National Natural Science Foundation of China under Grant 61875076, in part by the Fundamental Research Funds for the Central Universities under Grant 21619309, in by the Leading Talents of Guangdong Province Program under Grant 00201502, in part by the Natural Science Foundation of Guangdong Province under Grant 2019A1515011059, and in part by Open Fund of IPOC under Grant IPOC2019A001. Corresponding author: Ji Zhou (e-mail: zhouji@jnu.edu.cn).

Abstract: Orthogonal time-frequency-space (OTFS) modulation is a promising two-dimensional (2D) signal technique to tackle high mobility time-varying wireless channels. However, its good performance on time-frequency plane multiplexing for optical-wireless communications (OWC) has never been fully investigated. In this article, we take advantage of OTFS and propose a new orthogonal time-frequency multiplexing (OTFM) scheme for DC-biased OWC. We first design a 2D Hermitian symmetry in the DC-biased optical OTFM (DCO-OTFM) system to generate the real-valued signal. The bit error rate (BER) of a DCO-OTFM system is studied on the OWC channel. Numerical results demonstrate that the proposed scheme outperforms the conventional DC-biased optical orthogonal frequency division multiplexing scheme.

Index Terms: Orthogonal time-frequency multiplexing, 2D hermitian symmetry, optical-wireless communications.

1. Introduction

Orthogonal time-frequency-space (OTFS) modulation is an emerging solution to handle high Doppler shifts in time-varying multipath wireless channels [1]–[3]. Its key idea is to multiplex the data via two-dimensional (2D) orthogonal basis functions and place the functions in the delay-Doppler domain. Then the data can be transformed to the time-frequency domain with conventional modulation schemes, such as orthogonal frequency division multiplexing (OFDM). This promising technology, resulting in an improved bit error rate (BER), simplified channel estimation and signal detection in high-mobility scenarios, was first proposed in [1]. Subsequently, a series of work to improve the OTFS modulation system or expand its application scenarios has emerged. In [4], a low complexity OTFS structure was designed based on an OFDM system. [5]–[11] discuss novelty channel estimation, equalization and signal recovery schemes for OTFS system. The diversity performance of the OTFS signal was analyzed in [12]. In [13], OTFS modulation was first applied to a non-orthogonal multiple-access (NOMA) transmission protocol. In [14], the OTFS system was

proved to have excellent error performance on static multipath channels. In [15], the superiority of the peak-to-average power ratio (PAPR) of the OTFS signal compared to OFDM was analyzed.

Many researchers have proposed novel resource multiplexing and modulation techniques or devices for optical-wireless communications (OWC). Fujimoto and Lu, *et al.* [16] first designed a phase-modulated in-building network over fiber and invisible laser light communication transmission. In [17], free-space optical transmission was discussed under orbital-angular-momentum-multiplexed based on the spatial-mode multiplexing. In [18], a new modulation scheme based on a hybrid waveform was proposed for OWC of internet of vehicles. Among OWC topics, the study of optical OFDM has recently been a hotspot. Zhu *et al.* have proposed online service provisioning algorithms based on optical OFDM technology [19]. A PAPR reduction optimization method was designed in [20] for DC-biased optical OFDM (DCO-OFDM) visible light communications (VLC) systems. In [21], adaptive modulation combining several optical OFDM schemes was designed for VLC system. A hybrid system for VLC combined asymmetrically clipped optical orthogonal frequency division multiplexing (ACO-OFDM) and onoff keying modulation was proposed, which can accommodate various receivers with high spectral efficiency [22]. In [23], [24], different spatial dimming control schemes were proposed for DCO-OFDM VLC systems. X.Ling *et al.* provided a joint offset and power optimization method for a DCO-OFDM VLC system [25]. In [26], a 3D adaptive loading algorithm was proposed for a direct detection optical OFDM system. In [27], an improved receiver is designed for a layered ACO-OFDM (LACO-OFDM) OWC system. In [28], an adaptive modulation scheme based on LACO-OFDM was designed for the VLC system. In [29], fractional cosine transform based non-orthogonal frequency-division multiplexing was proposed for the VLC system to save more frequency resource than OFDM. In [30], a dual-polarization O-band silicon photonic transmitter is designed for direct detection OWC. In [31], an integration platform with novel plasmonic CMOS compatible TE-pass polarizer is presented for optical transmission. In [32], new structures of silicon photonic MachZehnder modulator are proposed for PAM-4 signal generation. To our best knowledge, research on OTFS system for OWC does not appear in the literature.

In this letter, we exploit the benefits of an OTFS system for performance improvement on static multipath channels, which is verified by [14] and can be adapted to OWC scenarios. Thus a new OWC scheme, Orthogonal Time-Frequency Multiplexing (OTFM), is proposed. We first develop a 2D Hermitian symmetry in the OTFM system to generate the real-valued signal, which enables the use of OTFM for the DC-biased OWC. Our proposed DC-biased optical OTFM (DCO-OTFM) system utilizes proper channel estimation and equalization method at the receiver side, which enables the demodulated signals to achieve better performance on BER and PAPR compared to an OFDM system.

The rest of this paper is outlined as follows. Section 2 introduces the OWC channel model and the DCO-OTFM system structure. In section 3, we propose 2D Hermitian symmetry in multiplexing in order to generate the transmitted real-valued signals. Section 4 discusses the channel equalization and demultiplexing in recovery. Section 5 presents the numerical results to demonstrate the scheme's performance. Finally, we present our conclusions in Section 6.

Notations: Throughout the letter, scalar, vector, and matrix are denoted by normal letters, lowercase boldface and uppercase boldface, respectively. The superscripts $(\cdot)^*$, $(\cdot)^T$ and $(\cdot)^H$ indicate conjugate, transpose, and conjugate transpose operations, respectively. We denote M-point discrete Fourier transform (DFT) and the inverse discrete Fourier transform (IDFT) operation matrices by $\mathbf{F}_M$ and $\mathbf{F}_M^H$.

2. Optical-Wireless Channel Model

We consider a DCO-OTFM system with single transmitter and receiver on the optical-wireless channel. Fig. 1 depicts the block diagram of DCO-OTFM for OWC system, which consists of necessary techniques in multiplexing and recovery. We assume that M subcarriers are allocated to transmit NM samples in an OTFM symbol on the duration NT_s, where T_s is the sampling interval. The OTFM symbols are transmitted over the optical-wireless channel, which the channel response

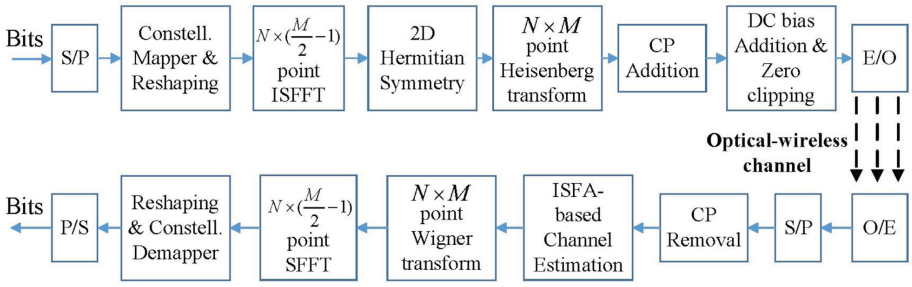

Fig. 1. Block diagram of DCO-OTFM system for OWC. S/P: series-to-parallel, P/S: parallel-to-series, CP: cyclic prefix, ISFA: intra-symbol frequency-domain averaging, E/O: electro/optic, O/E: optic/electro.

$h(\tau)$ is represented as follows:

$$h(\tau) = \sum_{p=0}^{P} h_p \delta(\tau - \tau_p), \tag{1}$$

where $(P+1)$ is the number of propagation multi-paths, and h_p with τ_p denotes the channel coefficient and the delay associated with the p-th propagation path. We consider the non-directed model of optical-wireless channel and employ the ceiling-bounce (CB) model to investigate the multipath effect on reflection light, which is similar to the channel model in [29]. Thus the impulse response of the CB model channel is shown as

$$h_{\text{cb}}(\tau) = \frac{6a^6}{(\tau + a)^7} u(\tau), \tag{2}$$

where $a = 12\sqrt{\frac{11}{13}}D$, D is the root-mean-square (RMS) delay spread of the multiple reflections, and $u(\tau)$ is the unit step function. So the received signal at OWC is represented as

$$y(t) = h_{\text{cb}}(\tau) * s(t) + n(t). \tag{3}$$

3. Real-Valued OTFM Signal Generation

We explain the multiplexing details in this section. As shown in the upper part of Fig. 1, similar to the modulation of OTFS, the information bits first must be reshaped as a constellation matrix after mapping operation, which is different from traditional DCO-OFDM. According to the subcarrier number in each OTFM symbol, the elements of the origin matrix formed by effective information constellation points is $x_{\text{o}}[k, l]$, where $k = 0, 1, \ldots, N-1$, and $l = 0, 1, \ldots, M/2-2$. Then the matrix is modulated with Inverse Symplectic Finite Fourier Transform (ISFFT), which can be expressed as

$$X_{\text{o}}[n, m] = \frac{2}{N(M-2)} \sum_{k=0}^{N-1} \sum_{l=0}^{M/2-2} x_{\text{o}}[k, l] e^{j2\pi\left(\frac{nk}{N} - \frac{2ml}{M-2}\right)}, \tag{4}$$

where $n \in 0, \ldots, N-1$ and $m \in 1, \ldots, M/2-1$. To ensure the time domain transmitted signals are real-valued, we first propose a new 2D Hermitian symmetry method on the signal matrix, which is developed from the Hermitian symmetry on optical OFDM real-valued systems. First we define an $N \times M$ matrix $\mathbf{X}$ as

$$\begin{cases} X[n, 0] = X[n, M/2] = 0, & n \in 0, \ldots, N-1, \\ X[n, m] = X_{\text{o}}[n, m], & n \in 0, \ldots, N-1, \quad m = 1, \ldots, M/2-1, \\ X[n, m] = X_{\text{o}}^{*}[n, M-m], & n \in 0, \ldots, N-1, \quad m = M/2+1, \ldots, M-1. \end{cases} \tag{5}$$

The frequency domain matrix $\mathbf{X}$ can be converted to the OTFM transmitted signal with Heisenberg transform. We take advantage of the method proposed in [14], which is achieved by M-point IDFT,

$$\bar{\mathbf{X}} = \sqrt{M}\mathbf{F}_M^H \mathbf{X}^T. \tag{6}$$

In the time domain signal matrix $\bar{\mathbf{X}}$, each element is

$$\begin{aligned}\bar{x}(n,m) &= \frac{1}{\sqrt{M}} \sum_{m=0}^{M-1} X[n,m] e^{j2\pi \frac{ml}{M}} \\ &= \frac{1}{\sqrt{M}} \left(\sum_{m=1}^{M/2-1} X[n,m] e^{j2\pi \frac{ml}{M}} + \sum_{m=M/2+1}^{M-1} X[n,m] e^{j2\pi \frac{ml}{M}} \right) \\ &= \frac{1}{\sqrt{M}} \sum_{m=1}^{M/2-1} \left(X[n,m] e^{j2\pi \frac{ml}{M}} + X^*[n,m] e^{-j2\pi \frac{ml}{M}} \right) \\ &= \frac{2}{\sqrt{M}} \sum_{m=1}^{M/2-1} \left(a(n,m) \cos\left(\frac{2\pi ml}{M}\right) - b(n,m) \sin\left(\frac{2\pi ml}{M}\right) \right). \end{aligned} \tag{7}$$

where $X[n,m] = a(n,m) + jb(n,m)$. After the matrix $\bar{\mathbf{X}}$ turns to vector $\bar{\mathbf{x}}$ with parallel to serial (P/S) conversion, a cycle prefix (CP) of length L is added to each symbol vector. The whole OTFM matrix $\check{\mathbf{X}}$ formed by K vectors after P/S conversion becomes a new baseband signal vector $\check{\mathbf{x}}$.

For the signal in the optical OFDM system in [33], a suitable DC bias is added to the bipolar transmitted signal, which makes the signal positive. Similarly, in this paper we set the biasing and clipping process on the bipolar OTFM signals, so the unipolar signal is defined as

$$s(t) = \begin{cases} \check{x}(t) + B_{\mathrm{DC}}, & \check{x}(t) > -B_{\mathrm{DC}} \\ 0, & \check{x}(t) \le -B_{\mathrm{DC}} \end{cases} \tag{8}$$

where B_{DC} is the DC bias and is associated with the power of $\check{x}(t)$,

$$B_{\mathrm{DC}} = \eta \sqrt{E[\check{x}(t)^2]}. \tag{9}$$

Then we define this bias as $10 \times \log_{10}(\eta^2 + 1)$dB. We can also study the statistical characterization of the real-valued DCO-OTFM with the help of expression (8), where the details are explained in section 5.

4. Receiver-Side Processing for OTFM Signal

In order to eliminate the inter-symbol interference (ISI) of our OTFM system, we apply frequency domain equalization on the receiver. As shown in the lower part of Fig. 1, the DC average component are first removed from the received electronic signals. After serial to parallel conversion and CP removal, we take the first I received OTFM symbols $\mathbf{y}_i$ as training symbols used for equalizer operation,

$$\hat{H}_i(j) = \frac{Y_i(j)}{X_i(j)}, \quad j = 0, 1, \ldots, N \times M - 1, \tag{10}$$

and the average estimated frequency domain channel response is defined as

$$\hat{H}(j) = \frac{1}{I} \sum_{i=1}^{I} \hat{H}_i(j), \quad j = 0, 1, \ldots, N \times M - 1. \tag{11}$$

From the definition in (5) we know that two subcarriers in each OTFM symbol carry no information signal, hence the two corresponding channels cannot be estimated. At the same time we reduce the overhead number of training symbols by applying the method of intra-symbol frequency-domain averaging (ISFA) [34]. The final estimated channel coefficient in frequency domain is get by

$$\hat{H}_{\mathrm{ISFA}}(j) = \begin{cases} 0, & j = 0, (NM)/2, \\ \sum_{r=j-s}^{j+s} \dfrac{\hat{H}(r)}{C_j}, & j_{\min} = 1,\ j_{\max} = (NM)/2 - 1,\ j \in [j_{\min},\ j_{\max}], \\ \sum_{r=j-s}^{j+s} \dfrac{\hat{H}(r)}{C_j}, & j_{\min} = (NM)/2 + 1,\ j_{\max} = NM - 1,\ j \in [j_{\min},\ j_{\max}], \end{cases} \tag{12}$$

where $C_j = \min(j_{\max}, j+s) - \max(j_{\min}, j-s) + 1$, and s is the number of left and right adjacent subcarriers employed for averaging.

With the received time domain signals $\mathbf{y}$ and estimated channel $\hat{H}_{\mathrm{ISFA}}$ we obtain the time domain vector $\hat{\mathbf{x}}$ to recover the final bits. We first turn each OTFM symbol vector into an $M \times N$ matrix $\hat{\mathbf{X}}$ and demodulate the matrix by Wigner transform, which can be seen as the inverse operation of Heisenberg transform. We obtain the estimated frequency domain matrix as:

$$\tilde{\mathbf{X}} = \frac{1}{\sqrt{M}} \mathbf{F}_M \hat{\mathbf{X}}, \tag{13}$$

which is a Hermitian symmetry matrix similar to $\mathbf{X}$. Then we use the signals on the effective subcarriers to form a new $N \times (M/2-1)$matrix $\hat{\mathbf{X}}_{\mathrm{o}}$, whose each element is defined as

$$\hat{X}_{\mathrm{o}}[u, v] = \tilde{X}^T[n, m],\ n = 0, \ldots, N-1,\ m = 1, \ldots, M/2-1, \tag{14}$$

where $u = 0, \ldots, N-1$, and $v = 0, \ldots, M/2-2$. We next demodulate the constellation value by SFFT with $\hat{\mathbf{X}}_{\mathrm{o}}$, where each estimated information signal is presented as:

$$\hat{x}_{\mathrm{o}}(k, l) = \sum_{u=0}^{N-1} \sum_{v=0}^{M/2-2} \hat{X}_{\mathrm{o}}[u, v] e^{-j2\pi\left(\frac{uk}{N} - \frac{2vl}{M-2}\right)}, \tag{15}$$

where $k = 0, \ldots, N-1$, and $l = 0, \ldots, M/2-2$. After constellation demapping we finally recover the received bits.

5. Simulation Setup and Results

In this section we present the simulation setup and compare the performance of OTFM with conventional OFDM for different QAM modulation. In all of the simulations, we consider 1024 samples transmitted in one OTFM symbol, where OTFM uses $M = 64$ subcarriers and $N = 16$ sampling time interval durations, respectively. To resist ISI, CP is $1/128$ the length of symbol duration, which means $L = 8$. $K = 128$ symbols form a DCO-OTFM frame, in which $I = 4$ symbols are set as training symbols for channel estimation overhead, and the other 124 symbols are information payload.

We first analyze the BER performance of OTFM schemes. Fig. 2(a) shows BER versus the SNR for DCO-OTFM and DCO-OFDM, where the DC bias is set to 7 dB and the transmission rate for the signals is 100 Mbit/s. The CB channel RMS delay spread is set to 10 ns. Each DCO-OFDM symbol transmits 1024 samples with 1024 subcarriers, and other parameters are set the same as for the DCO-OTFM signals. The required SNRs of DCO-OTFM to achieve the threshold of BER, i.e, BER of 1×10^{-3}, are lower than for DCO-OFDM in both 4QAM and 16QAM. In 4QAM the required SNR difference between DCO-OTFM and DCO-OFDM is about 3 dB. In 16QAM mode, the BER of OTFM outperforms that of OFDM at a SNR of 34 dB and reaches the threshold at 40 dB.

In Fig. 2(b), we demonstrate the BER against SNR with different RMS delay spread for 4QAM DCO-OTFM and DCO-OFDM, setting the DC bias at 7 dB and transmission rate at 100 Mbit/s. All of the values of RMS delay spread are chosen from the typical range for practical OWC scenarios.

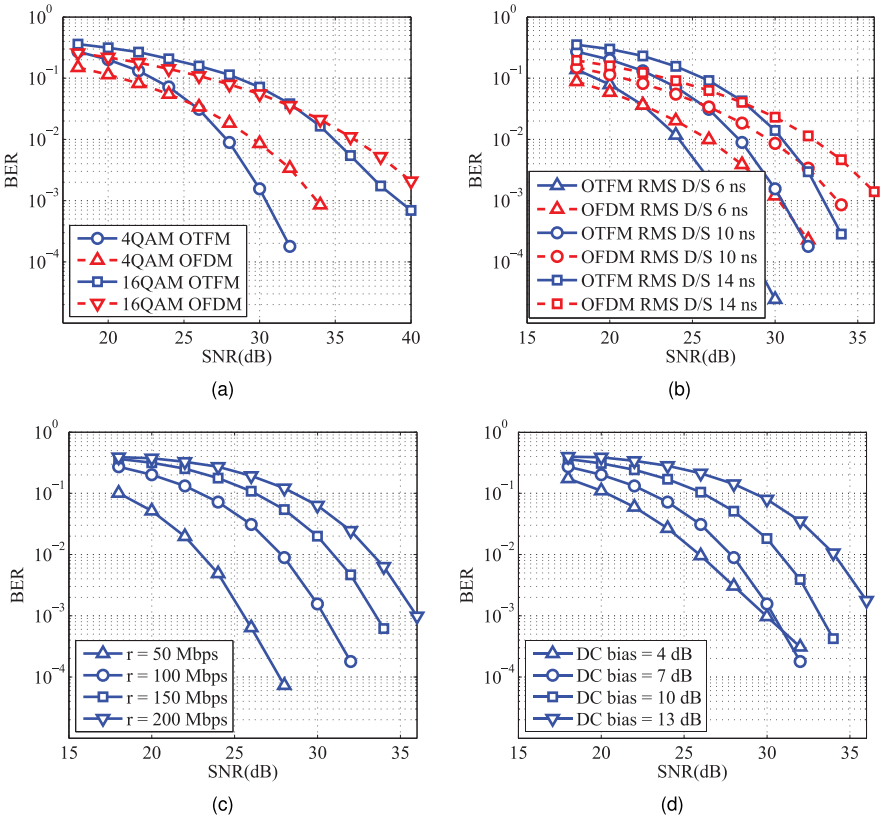

Fig. 2. BER performance versus the SNR for DCO-OTFM and DCO-OFDM. (a) BER against the SNR for different QAM, $r = 100$ Mbps, RMS delay spread 10 ns, DC bias 7 dB. (b) BER against the SNR for different RMS delay spread on 4QAM DCO-OTFM and DCO-OFDM, D/S: delay spread. (c) BER against the SNR for different transmission rate on 4QAM DCO-OTFM. (d) BER against the SNR for different DC bias on 4QAM DCO-OTFM.

The BER performance becomes worse with the increase of the RMS delay spread as a result of the decrease of the channel bandwidth. When the RMS delay spread is set to 14 ns, the SNR required to achieve the BER threshold is about 33 dB, which is 3 dB more than the required SNR with the 10-ns RMS delay spread. The BER performance of DCO-OFDM are worse than DCO-OTFM with the same RMS delay spread values, which also verifies our results in Fig. 2(a).

Fig. 2(c) compares the BER performance with different transmission rate under 7-dB DC bias and 10-ns RMS delay spread. The performance deteriorates with the increase of the rate as the consequence of the decrease of the sampling interval T_s. Furthermore, when the transmission rate doubles, which means sampling time T_s is reduced by half, the channel impulse response of the CB model channel cut down approximately half under normalized energy. Thus we need to raise the power by almost the same value in dB to compensate the loss when the data rate doubles. For example, our simulation results show the difference of SNR from 50 Mbps to 100 Mbps and from 100 Mbps to 200 Mbps for the required BER is just about 5 dB, which means the OTFM can be applied to different speed transmission scenarios.

We next illustrate the BER versus SNR with different DC bias in Fig. 2(d), where other parameters are set the same as in Fig. 2(a). In the DCO-OTFM system, BER suffers from clipping distortion, which decreases with the increase of DC bias. If the DC bias is large enough, there is almost no clipping noise in DCO-OTFM. The difference between the required SNRs for DCO-OTFM with different DC bias is equal to the difference between the corresponding DC-bias power. When the DC bias is set to 4 dB, the signal suffers the clipping noise, hence the difference between the required SNRs of DCO-OTFM with 4- and 7-dB DC bias is less than 3 dB. Even the performance

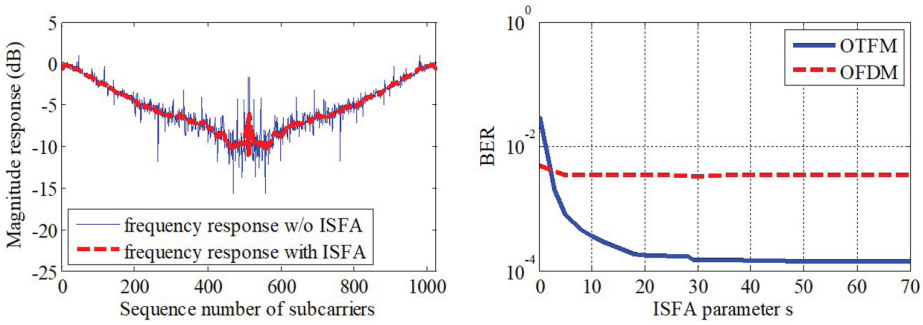

Fig. 3. Performance improvement for OTFM with ISFA technique. (a) Frequency magnitude response of estimated channel for OTFM, w/o: without. (b) BER for 4QAM in different ISFA parameters, SNR = 32 dB.

with 4-dB DC bias is worse than with 7-dB DC bias on some particular SNRs. However, the differences between the required SNRs of DCO-OTFM with 7-, 10- and 13-dB DC bias are almost equal to 3 dB due to little clipping noise in the signal when the DC bias is larger than 7 dB. The simulation results in Fig. 2(d) coincide with the theoretical analysis.

Fig. 3 depicts the influence of the ISFA technique on the 4QAM OTFM signals with a SNR of 32 dB. In Fig. 3(a), we set the ISFA parameter as $s = 20$ to apply ISFA on the estimated channel frequency response, and blue curve is processed with (12) to get the red curve. The average value of red line and blue line are -5.23 and -5.22 respectively, which are almost the same. However, the blue line values' variance and its gradients' variance are 9.14 and 0.63, and the same time the relative variances of red line are 8.20 and 0.06, which is smaller than the blue line's. This comparison verifies that the red curve is smoother than the blue one, which is shown in Fig. 3(a). Frequency response with ISFA helps the estimation phase take less OTFM symbols for training in order to save the overhead. Fig. 3(b) further shows the improvement in demodulation with the ISFA technique. We compare the BER of OTFM and OFDM with different ISFA parameters s with the same SNR, where $s = 0$ means ISFA is not applied. It is depicted that when the SNR is set to 32 dB the BER of OTFM is worse than for OFDMs without ISFA. With s increasing the performance is rapidly improved, and OTFM outperforms OFDM when the parameter is properly chosen (i.e. $s \geq 20$).

Fig. 4 shows the constellation coordinates of the received signal after channel estimation and OTFM demultiplexing. Fig. 4(a) and (b) demonstrate the 4QAM and 16QAM signals with SNRs of 32 dB and 40 dB, respectively. Both pictures obviously reflect that most demultiplexing signals' coordinates are close to the standard QAM constellation points' coordinates, which helps the demapper to accurately recover the information bits.

Though many references such as [14] and [15] have proved the improvement of PAPR by OTFS through theoretical analysis or simulation verification, we further demonstrate simulation comparison between OTFS symbol and OFDM symbol in the same conditions. The analysis of the PAPR property of the OTFM signal helps us set the proper parameters to design an OTFM symbol. In Fig. 5(a), we compare the PAPR of OTFM and OFDM in 4QAM signals to display the superiority of OTFM. We consider the complementary cumulative distribution function (CCDF) of concatenation of 10000 symbols for two systems, where all of the symbols have 1024 samples. It is shown that OTFM has better PAPR than OFDM system, and this superiority will improve when we decrease the sampling interval number of OTFM symbols. For example, OTFM's PAPR is approximately 0.9 dB lower than that of OFDM at a probability of 10^{-4} in the 4QAM signal, when $N = 8$, $M = 128$, which is lower than with $N = 16$, $M = 64$ at the same probability. The results coincide with the conclusions of the above references, and confirm that our chosen parameters for OTFM are proper to show the superiority in both BER and PAPR performance.

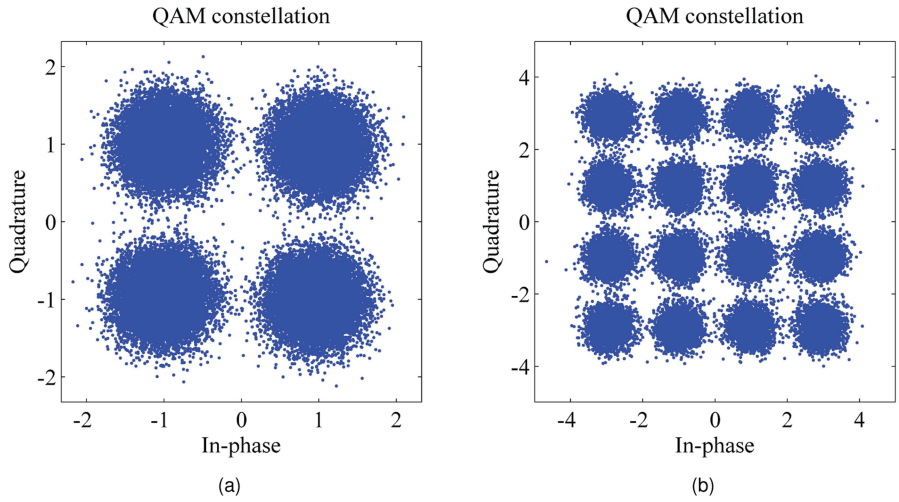

Fig. 4. Constellation coordinates of demultiplexing OTFM signals. (a) 4QAM, SNR = 32 dB. (b) 16QAM, SNR = 40 dB.

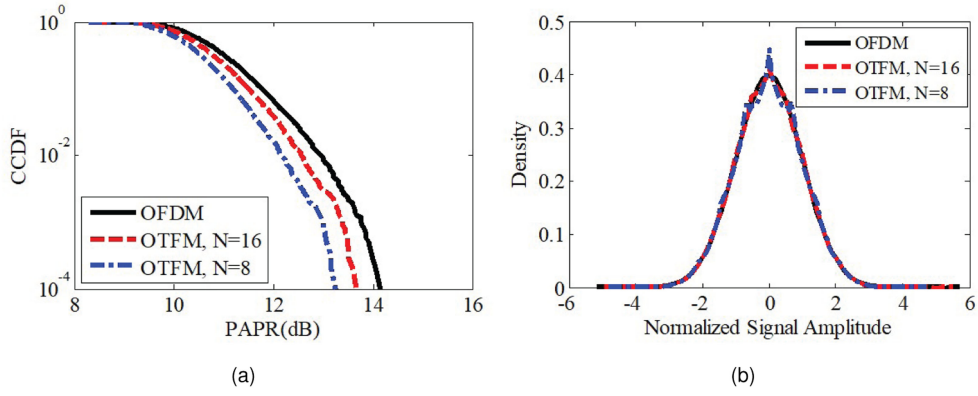

Fig. 5. Comparision of PAPR between OTFM and OFDM. (a) CCDF of PAPR of OTFM and OFDM. (b) PDF of time domain signals of OTFM and OFDM.

Fig. 5(b) illustrates the statistical characteristics of time domain OTFM signals with 4QAM. The analysis is performed like those in [33]. The mean of bipolar OTFM symbols $\check{\mathbf{x}}$ is almost zero. The real-valued time domain signal $\check{x}(t)$ is normalized such that the empirical variance is equal to one, which suggests that we can model the $\check{x}(t)$ sequence using an i.i.d. Gaussian process with the following probability density function (pdf),

$$pdf_{\check{x}}(x) = \mathcal{N}(x; 0, \sigma^2), \tag{16}$$

$$\mathcal{N}(x; \mu, \sigma^2) = \frac{1}{\sqrt{2\pi}\sigma} e^{-\frac{(x-\mu)^2}{2\sigma^2}}, \tag{17}$$

where μ and σ^2 are the respective mean and variance of the Gaussian distribution. The simulation results of the probability density distribution in Fig. 5(b) compare the difference between OTFM and OFDM in the time domain. When $N = 16$, the distribution curve of OTFM is almost the same as that of OFDM, where the latter's pdf also belongs to Gaussian process. When $N = 8$, more signals distribute around the mean of OTFM symbols and the range of magnitude is smaller than that of OFDM. It also explains why the OTFM shows better PAPR performance.

6. Conclusion

In this paper, a DCO-OTFM scheme was proposed for an OWC system. We first designed a 2D Hermitian symmetry in multiplexing to generate the real-valued OTFM signal. In signal recovery, we applied frequency domain equalization with an ISFA-based method to resist the ISI. Numerical results show that our proposed schemes perform significantly better than the conventional DCO-OFDM scheme in BER, especially when the OTFM signals were recovered with proper ISFA parameters. We also analyzed the proper design of OTFM to improve the performance of PAPR compared with the OFDM system. All of the results revealed that the proposed DCO-OTFM system satisfies the needs of practical OWC scenarios. Future works may be carried out on an MIMO OTFM OWC system and DCO-OTFM NOMA uplink communications, etc.

References

[1] R. Hadani *et al.*, "Orthogonal time frequency space modulation," in *Proc. IEEE Wireless Commun. Netw. Conf.*, San Francisco, CA, USA, Mar. 2017.

[2] R. Hadani and A. Monk, "OTFS: A new generation of modulation addressing the challenges of 5G," 2018, *arXiv: 1802.02623.*

[3] R. Hadani *et al.*, "Orthogonal time frequency space modulation," 2018, *arXiv: 1808.00519*.

[4] A. Farhang, A. RezazadehReyhani, L. E. Doyle, and B. F.-Boroujeny, "Low complexity modem structure for OFDM-based orthogonal time frequency space modulation," *IEEE Wireless Commun. Lett.*, vol. 7, no. 3, pp. 344–347, Jun. 2018.

[5] P. Raviteja, K. T. Phan, and Y. Hong, "Embedded pilot-aided channel estimation for OTFS in delay-Doppler channels," *IEEE Trans. Veh. Technol.*, vol. 68, no. 5, pp. 4906–4917, May 2019.

[6] W. Shen, L. Dai, J. An, P. Fan, and R. W. Heath, Jr,"Channel estimation for orthogonal time frequency space massive MIMO," *IEEE Trans. Signal Process.*, vol. 67, no. 16, pp. 4204–4217, Aug. 2019.

[7] J. Cheng, H. Gao, W. Xu, Z. Bie, and Y. Lu, "Low-complexity linear equalizers for OTFS exploiting two-dimensional fast Fourier transform," 2019, *arXiv: 1909.00524*.

[8] S. Tiwari, S. S. Das, and V. Rangamgari, "Low complexity LMMSE receiver for OTFS," *IEEE Commun. Lett.*, vol. 23, no. 12, pp. 2205–2209, Dec. 2019.

[9] L. Li, Y. Liang, P. Fan, and Y. Guan, "Low complexity detection algorithms for OTFS under rapidly time-varying channel," in *Proc. IEEE 89th Veh. Technol. Conf. (VTC2019-Spring)*, Jun. 2019, pp. 1–5.

[10] F. Long, K. Niu, C. Dong, and J. Lin, "Low complexity iterative LMMSE-PIC equalizer for OTFS," in *Proc. IEEE Int. Conf. Commun.*, May 2019, pp. 1–6.

[11] M. Zhang, F. Wang, X. Yuan, and L. Chen, "2D structured turbo compressed sensing for channel estimation in OTFS systems," in *Proc. IEEE Int. Conf. Commun. Sys.*, Dec. 2018, pp. 45–49.

[12] H. Zhang, X. Huang, and J. A. Zhang, "Comparison of OTFS diversity performance over slow and fast fading channels," in *Proc. IEEE/CIC Int. Conf. Commun. in China*, Dec. 2019, pp. 828–833.

[13] Z. Ding, R. Schober, P. Fan, and H. Vincent Poor, "OTFS-NOMA: An efficient approach for exploiting heterogenous user mobility profiles," *IEEE Trans. Commun.*, vol. 67, no. 11, pp. 7950–7965, Nov. 2019.

[14] P. Raviteja, E. Viterbo, and Y. Hong, "OTFS performance on static multipath channels," *IEEE Wireless Commun. Lett.*, vol. 8, no. 3, pp. 745–748, Jun. 2019.

[15] G. D. Surabhi, R. M. Augustine, and A. Chockalingam, "Peak-to-average power ratio of OTFS modulation," *IEEE Commun. Lett.*, vol. 23, no. 6, pp. 999–1002, Jun. 2019.

[16] D. Fujimoto, H. Lu, K. Kumamoto, S. Tsai, Q. Huang, and J. Xie, "Phase-modulated hybrid high-speed internet/WiFi/Pre-5G in-building networks over SMF and PCF with GI-POF/IVLLC transport," *IEEE Access* vol. 7, pp. 90620–90629, Jul. 2019.

[17] B. B. Yousif and E. E. Elsayed, "Performance enhancement of an orbital-angular-momentum-multiplexed free-space optical link under atmospheric turbulence effects using spatial-mode multiplexing and hybrid diversity based on adaptive MIMO equalization," *IEEE Access*, vol. 7, pp. 84401–84412, Jun. 2019.

[18] M. D. Thieu, T. L. Pham, T. Nguyen, and Y. M. Jang, "Optical-RoI-signaling for vehicular communication," *IEEE Access*, vol. 7, pp. 69873–69891, May 2019.

[19] Z. Zhu, W. Lu, L. Zhang, and N. Ansari, "Dynamic service provisioning in elastic optical networks with hybrid single-/multi-path routing," *J. Lightw. Technol.*, vol. 31, no. 1, pp. 15–22, Jan. 2013.

[20] H. Zhang, Y. Yuan, and W. Xu, "PAPR reduction for DCO-OFDM visible light communications via semidefinite relaxation," *IEEE Photon. Technol. Lett.*, vol. 26, no. 17, pp. 1718–1721, Sep. 2014.

[21] L. Wu, Z. Zhang, J. Dang, and H. Liu, "Adaptive modulation schemes for visible light communications," *J. Lightw. Technol.*, vol. 33, no. 1, pp. 117–125, Jan. 2015.

[22] F. Yang, J. Gao, and S. Liu, "Novel visible light communication approach based on hybrid OOK and ACO-OFDM," *IEEE Photon. Technol. Lett.*, vol. 28, no. 14, pp. 1585–1588, Jul. 2016.

[23] Y. Yang, Z. Zeng, J. Cheng, and C. Guo, "Spatial dimming scheme for optical OFDM based visible light communication," *Opt. Express*, vol. 24, no. 26, pp. 30254–30263, Dec. 2016.

[24] Z. Feng, C. Guo, Z. Ghassemlooy, and Y. Yang, "The spatial dimming scheme for the MU-MIMO-OFDM VLC system," *IEEE Photon. J.*, vol. 10, no. 5, Oct. 2018, Art. no. 7907013.

[25] X. Ling, J. Wang, X. Liang, Z. Ding, and C. Zhao, "Offset and power optimization for DCO-OFDM in visible light communication systems," *IEEE Trans. Signal Process.*, vol. 64, no. 2, pp. 349–362, Jan. 2016.
[26] X. Chen *et al.*, "Three-dimensional adaptive modulation and coding for DDO-OFDM transmission system," *IEEE Photon. J.*, vol. 9, no. 2, Apr. 2017, Art. no. 6600720.
[27] Q. Wang, Z. Wang, X. Guo, and L. Dai, "Improved receiver design for layered ACO-OFDM in optical wireless communications," *IEEE Photon. Technol. Lett.*, vol. 28, no. 3, pp. 319–322, Feb. 2016.
[28] Y. Sun and F. Yang, "Adaptive modulation scheme based on partially pre-distorted LACO-OFDM for VLC system," *IEEE Photon. J.*, vol. 11, no. 5, Oct. 2019, Art. no. 7906312.
[29] J. Zhou *et al.*, "Faster-than-nyquist non-orthogonal frequency-division multiplexing for visible light communications," *IEEE Access*, vol. 6, pp. 17933–17941, Mar. 2018.
[30] E. El-Fiky *et al.*, "200 Gb/s transmission using a dual-polarization O-Band silicon photonic intensity modulator for Stokes vector direct detection applications," *Opt. Express*, vol. 25, no. 24, pp. 30336–30348, Nov. 2017.
[31] N. Abadía *et al.*, "CMOS-compatible multi-band plasmonic TE-pass polarizer," *Opt. Express*, vol. 26, no. 23, pp. 30292–30304, Nov. 2018.
[32] A. Samani *et al.*, "Silicon photonic Mach-Zehnder modulator architectures for on chip PAM-4 signal generation," *J. Lightw. Technol.*, vol. 37, no. 13, pp. 2989–2998, Jul. 2019.
[33] J. Zhou, Y. Qiao, Z. Cai, and Y. Ji, "Asymmetrically clipped optical fast OFDM based on discrete cosine transform for IM/DD systems," *J. Lightw. Technol.*, vol. 33, no. 9, pp. 1920–1926, May 2015.
[34] X. Liu and F. Buchali, "Intra-symbol frequency-domain averaging based channel estimation for coherent optical OFDM," *Opt. Express*, vol. 16, no. 26, pp. 21944–21957, Dec. 2008.